

Mechanical and Ka-Band Electrical Reliability Testing of Interconnects in 5G Wearable System-on-Package Designs Under Bending

Yi Zhou¹, Kexin Hu², Manos M. Tentzeris², and Suresh K. Sitaraman¹

¹George W. Woodruff School of Mechanical Eng.
Flexible Wearable Electronics Advanced Research
Georgia Institute of Technology
Atlanta, GA, USA
email: suresh.sitaraman@me.gatech.edu

²School of Electrical and Computer Eng.
Georgia Institute of Technology
Atlanta, GA, USA

Abstract—Additive printing is being increasingly used for the fabrication of flexible electronics. Low-loss interconnects are required to achieve heterogeneous integration for 5G/mm-wave electronics packaging. In addition, the packaged systems need to have good mechanical and electrical reliability under bending conditions and survive from a large number of cyclic bending to be applied under flexible conditions. A microstrip line is designed and inkjet printed on a 3D printed polypropylene (PP) substrate. Three different metallization thicknesses of printed ink structures, 3 layers (6.13 μm), 6 layers (9.52 μm), and 9 layers (14.82 μm), are fabricated for characterization. Nine-layer microstrip line samples have the lowest insertion loss (less than 0.08 dB/mm) over 20–40 GHz. The maximum loss measured at bending condition is 0.17 dB/mm when the 3-layer samples are bent over the smallest mandrel with radius of 1 in. In the cyclic bending test over a mandrel with a radius of 1 in., 6-layer samples are able to maintain < 0.10 dB/mm loss before 10000 cycles. Scanning electron microscopy (SEM) images show that thicker printed ink tends to have more micro defects formed during fabrication, and cracks grow longer as more numbers of bending cycles are performed. As the loading is similar among samples of different thicknesses, based on mechanical finite-element analysis (FEA) simulations, the original defects from fabrication dominate the reliability of microstrip lines. Ramp interconnects are designed and fabricated, and each interconnect features 0.1–0.5 dB insertion loss over 20–32 GHz. Preliminary bending tests with a bending radius of 1 in. show that the ramp interconnect has no physical changes up to 10000 bending cycles.

Keywords—flexible hybrid electronics; additive manufacturing; 3D printing; inkjet printing; 5G interconnects; microstrip lines; 3D interconnect; mandrel bending

I. INTRODUCTION

Next-generation 5G/mm-wave wearable smart devices require reliable performance within a broad bandwidth [1], low parasitic losses at mm-wave frequencies [2], high volumetric utilization so that more functionalities can be packed into a compact module [3], and good mechanical flexibility so that they can conform to curvatures on body [4]. System-on-Package (SoP) is a 3D stack-up packaging solution to overcome the challenges of 5G flexible electronics device, which focuses on integrating ICs with other active and passive components within a multi-layer and multi-material package [5].

The conventional clean-room fabrication process has limitation on handling gradient materials and creating non-planar structures. Thus, additive manufacturing (printing) is a promising state-of-art process which can be used to fabricate highly integrated flexible wireless systems [6]. 3D printing is an emerging technology that prints materials layer by layer to form an object directly from a 3D computer aided design (CAD). The flexibility and efficiency in manufacturing that 3D printing provides, make it widely applied as a solution for customization in industries [7]. In this work, polypropylene (PP) is printed using a 3D printer to serve as the substrate for the printed electronics components. The PP substrate is characterized to be low-loss (loss $\tan \delta = 0.001$) in mm-wave that mitigates dielectric loss in in-package interconnects. Inkjet printing is a popular fabrication method in flexible electronics, as it is a maskless drop-on-demand method, which provides engineers and researchers more flexibility in design process [8]. Two materials are used for inkjet printing in the fabricated samples for this work: SU-8 and SunTronic EMD5730 silver nanoparticle ink.

There are many challenges faced by the interconnects in packaging of flexible 5G system. In the mm-wave designs, interconnections between ICs, passives, antennas, and other components should have low insertion loss over the frequency range of interest [9]. In this work, microstrip lines that are inkjet printed onto 3D printed PP substrates are targeting to have insertion loss less than 0.2 dB/mm over 20–40 GHz at all times. Ramp interconnect [10,11], an IC interconnect structure is also fabricated using inkjet printing. The insertion loss for a single ramp interconnect is aimed to be less than 0.5 dB over 20–40 GHz. During application, a flexible/wearable electronics system might undergo deformations due to stretching, bending and/or twisting uniaxially or biaxially. Reliability tests are developed to study the mechanical and electrical behaviors of the flexible electronics when it is subjected to such deformations [12–25]. Since the proposed application for the design in this work is a wristband, the mechanical and electrical reliability of the microstrip line and ramp interconnect will be studied under mandrel bending down to radius of 1 in. and bending up to 10000 cycles. Scanning electron microscopy (SEM) images and finite-element analysis (FEA) model are used to facilitate the investigation of failure mechanism of the printed interconnects.

II. MICROSTRIP LINES DESIGN, FABRICATION AND MEASUREMENTS

A. Microstrip Line Design and Fabrication

The evaluation of interconnects starts from the most basic microstrip line structure. The substrate of microstrip line is chosen to be 3D printed polypropylene (PP), which is printed from a FDM (Fused Deposition Modeling) 3D printer, Ultimaker S3, with Ultimaker PP filament as shown in Fig. 1a and Fig. 1b. However, it has been noticed that PP substrates cannot be directly used for inkjet printing as printed silver ink becomes scattered dots rather than a continuous line when deposited onto it. To improve the surface wetting, the substrates require certain surface treatment. First, UVO (ultraviolet-ozone) cleaning is necessary to remove contaminants and make plastic surfaces more hydrophilic. The optimal duration for UVO treatment is decided to be three minutes based on numerous experiments. Then, two layers of SU-8 are inkjet printed on the substrates to work as buffer layers for silver ink in order to achieve good ink adhesion. Fig. 1c shows a sample with 3D printed PP substrate and inkjet printed silver trace on SU-8 buffer layers. SU-8 is a transparent material, so that it is not seen in Fig. 1c. Fig. 2 shows the inkjet printer Dimatix Materials Printer DMP-2850 used to print both SU-8 and the silver nano particle ink.

The RF characterization of 3D printed PP has been conducted through transmission/reflection method, and dielectric constant and loss tangent are derived from Nicolson-Ross-Weir (NRW) method. The design parameters are shown in Table I. The line width of microstrip line is 0.55 mm on 0.2 mm thick PP substrate to achieve impedance matching of 50 Ω . For each microstrip line sample, Suntronic silver nanoparticle ink EMD5730 is used and printed by Dimatix Materials Printer DMP-2850. The printed silver ink

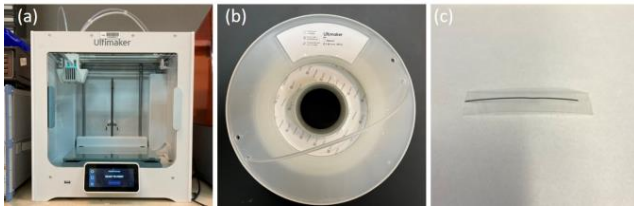


Figure 1. Polypropylene (PP) substrates are fabricated by the Ultimaker S3 3D printer presented in a), and using polypropylene filament produced by Ultimaker shown in b). A sample 3D printed PP substrate with inkjet printed silver structure is presented in c).



Figure 2. Inkjet printer used to print SU-8 and Suntronic ink.

TABLE I. MICORSTRIP LINE DESIGN PARAMETERS

Dielectric Constant*	2.34
Loss Tangent*	0.001
Substrate Thickness	0.20 mm
Surface Roughness*	0.063 sq/ μ m
Line Length	60.00 mm
Line Width	0.55 mm
SU-8 Width	2.00 mm

* in-house measurement: dielectric constant and loss tangent are derived by NRW method, and surface roughness is measured by a profilometer.

is cured in a thermal oven at 130 $^{\circ}$ C for 1 hr with the temperature of the oven ramping from 60 $^{\circ}$ C to 130 $^{\circ}$ C in 15 min. Upon curing at 130 $^{\circ}$ C for 1 hr, the temperature is ramped down to 60 $^{\circ}$ C in 15 min. The gradual ramping down is necessary to reduce excessive warpage and/or cracking of the printed ink. Additionally, the printed samples are taped down by Kapton tape to a thick glass plate in the oven to limit the deformation of samples caused by different coefficients of thermal expansion between different materials. At least three layers of silver ink is inkjet printed on each substrate sample to ensure the metallization thickness (\sim 6.13 μ m) is greater than the maximum skin depth of 1.18 μ m over 24-40 GHz. Also, it is observed that increasing the number of layers of printed silver ink would result in higher conductivity. Therefore, in this work, three different metallization thickness: 3 layers, 6 layers and 9 layers of silver ink are tested for the microstrip line samples. After printing each layer, the silver trace is heated up by hot gun for a short amount of time to prevent ink spreading. In addition, 3M copper tapes are used as the ground plane of microstrip line samples. The total length of the sample is designed to be 60 mm, while the width of the substrate and the ground plane is 15 mm, and the width of SU-8 layer is 2 mm.

B. Microstrip Line Visual Inspections

Top view: Fig. 3a shows the fabricated microstrip lines. The top side of the PP substrate has a straight line in the middle, which is the printed silver ink, while the bottom part of the substrate has the copper tape attached to it. Since PP substrate and SU-8 layer are transparent, the copper tape is seen through as shown in Fig. 3a. Fig. 3b indicates the stacking information in top view, where it is seen that between the silver ink structure and PP substrate, there is an SU-8 layer. The actual geometry details of the fabricated microstrip are obtained from optical inspections.

Cross-section view: Fig. 3c shows the microscopic inspection results of the cross section of a 6-layer microstrip sample. The bottom layer is the copper tape ground plane of 119.00 μ m, and the second from the bottom layer is the 3D printed PP of 230.14 μ m. The third from the bottom layer is inkjet printed SU-8 layer, which is measured to be 16.03 μ m thick and 2123.65 μ m wide. The stacking information of the fabricated microstrip lines of cross-sectional view is shown in Fig. 3c and 3d. It is noticed that the cross section of the SU-8 layer is approximately an isosceles trapezoidal shape rather than a rectangular shape, where there is a base angle of 2.68 $^{\circ}$ in both sides as shown. The top layer is the inkjet

printed silver layer, and its cross section is of isosceles trapezoidal shape as well. The silver ink layer thickness is of 6.13 μm for 3-layer sample, 9.52 μm for 6-layer sample, and 14.82 μm for 9-layer. The width of the silver layer is also different in samples of different thickness due to the ink spreading issue. 3-layer microstrip line has total width of 502.51 μm and base angle of 5.02°; 6-layer microstrip line has total width of 571.60 μm and base angle of 6.42°; and 9-layer microstrip line has total width of 564.99 μm and ramp width of 7.04°. Fig. 3e and 3f show details of base angle of SU-8 and silver ink layers. The geometry details are summarized in Table II.

C. Microstrip Line Measurements

In total four sets of microstrip samples are prepared. Each set includes one 3-layer, one 6-layer, and one 9-layer

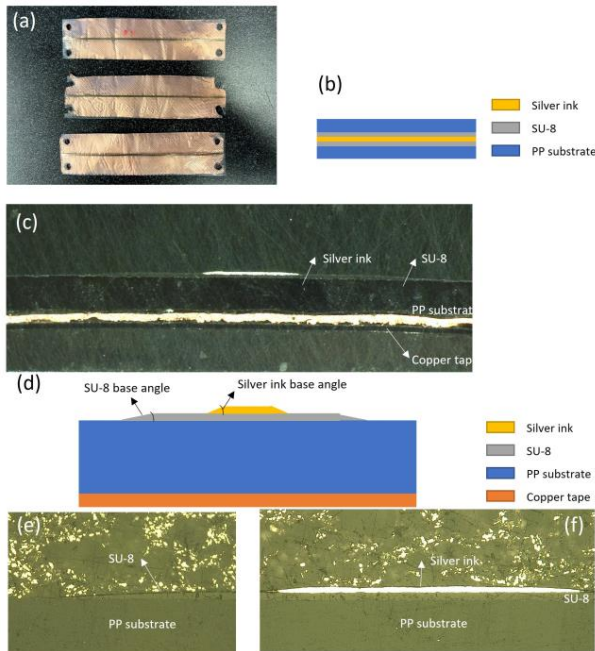


Figure 3. Visual inspections of the printed microstrip samples: a) top view of three samples with different printed ink thickness; b) stacking information of the microstrip line samples in top view; c) cross-section of a 6-layer microstrip sample; d) stacking information of the microstrip line samples in cross sectional view; e) zoomed-in of cross-section of SU-8 layer near its left edge; and f) zoomed-in of cross-section of silver ink layer on top of SU-8 layer and PP substrate.

TABLE II. GEOMETRY MEASUREMENTS OF MICROSTRIP LINE SAMPLES

Ink base angle	5.04° (3-layer)
	6.42° (6-layer)
	7.04° (9-layer)
Ink thickness	6.13 μm (3-layer)
	9.52 μm (6-layer)
	14.82 μm (9-layer)
Ink width	502.51 μm (3-layer)
	571.60 μm (6-layer)
	564.99 μm (9-layer)
SU-8 base angle	2.68°
SU-8 width	2123.65 μm
SU-8 thickness	16.03 μm
PP thickness	230.14 μm
Copper thickness	119.00 μm

samples. The RF measurements are performed using an Anritsu MS46522B Vector Network Analyzer (VNA), which is calibrated with an Anritsu K Calibration Kit Model 3652A, using the SOLT (Short-Open-Load-Thru) standards [26]. Fig. 4a plots the average de-embedded S_{21} measurement results for different types of samples with error bars indicating the standard deviation at 24 GHz, 28 GHz, 32 GHz, 36 GHz, and 40 GHz, which are significant frequencies for 5G NR (New Radio) bands. The insertion loss values and the conductivity of the ink of 3-layer, 6-layer, and 9-layer samples are summarized in Table III. It can be seen that 9-layer samples

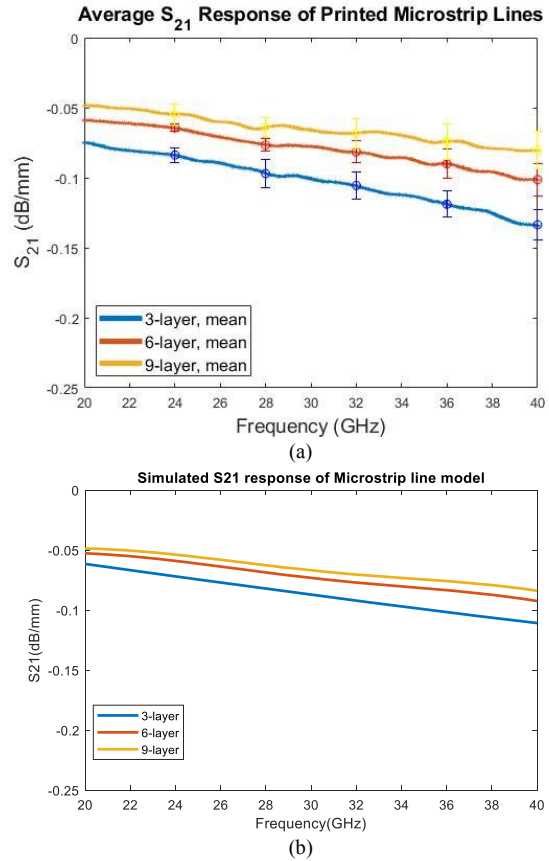


Figure 4. (a) Measured average S_{21} responses of four sets of 3-layer, 6-layer, and 9-layer samples; (b) simulated S_{21} responses of 3-layer, 6-layer, and 9-layer samples.

TABLE III. SUMMARY OF INSERTION LOSS AND CONDUCTIVITY VALUES

	3-Layer	6-Layer	9-Layer
Average Insertion Loss 20-40 GHz (dB/mm)	0.074	0.059	0.048
Standard Deviation at 24 GHz (dB/mm)	-0.130	-0.101	-0.080
Standard Deviation at 28 GHz (dB/mm)	0.005	0.003	0.007
Standard Deviation at 32 GHz (dB/mm)	0.010	0.004	0.007
Standard Deviation at 36 GHz (dB/mm)	0.009	0.008	0.011
Standard Deviation at 40 GHz (dB/mm)	0.009	0.010	0.012
Conductivity ($\times 10^6 \text{ S/m}$)	0.011	0.012	0.013
	1.808	4.440	7.590

have the lowest insertion loss of all the samples of different ink thickness, and all samples demonstrate that the insertion loss is well below 0.2 dB/mm. The lowest loss for the 9-layer ink is due to its highest conductivity of all thicknesses, and the overall loss being less than 0.2 dB/mm for all ink thicknesses is due to the low-loss tangent feature of PP substrate. It is also noted that the standard deviations in insertion loss increase as the frequency increases because higher frequencies are more sensitive to surface imperfections. The values of standard deviation of all three sample thicknesses are similar and relatively small, which indicates good repeatability in the sample fabrication. The simulated S_{21} in CST Studio Suite is presented in Fig. 4b. The measured S_{21} matches well with simulation results and the main deviation may be caused by imperfect surface condition and ink defects.

III. MICROSTRIP RELIABILITY TESTS AND RESULTS

A. Monotonic Mandrel Bending Test Over Different Sizes of Mandrel

It is critical to evaluate the electrical performance of microstrip line under bending; therefore, the microstrip lines (a 3-layer, a 6-layer, and a 9-layer) are tested in the monotonic mandrel bending experiment over different sizes of mandrels. Four sizes of polycarbonate cylindrical mandrels with an outer radius of 4, 3, 2, and 1 in. are used as seen in Fig 5a. At the start of the bending experiments, the VNA is used to measure S_{21} of the microstrip line in the flat configuration as seen in Fig. 5b. After the flat-configuration measurements, the microstrip lines are sequentially wrapped around the mandrel from the largest size to the smallest size to measure the S_{21} as seen in Fig. 5c. After all the bending is done, the sample is measured again at flat condition. This experimental procedure would minimize potential damage to the printed structure. In all the experiments, the sample is wrapped such that the ink layer would face outward, and therefore, circumferential tensile strain is applied on the silver ink layer.

The S_{21} measurement results of the monotonic mandrel bending test are presented in Fig. 6. Before bending, in the frequency range of 20-40 GHz, the 3-layer microstrip line sample has insertion loss ranging from 0.075 to 0.136 dB/mm, the 6-layer sample has insertion loss ranging from 0.061 to 0.118 dB/mm, and the 9-layer sample has insertion loss ranging from 0.048 to 0.095 dB/mm, for the one set of samples. All three samples show the same trends in their

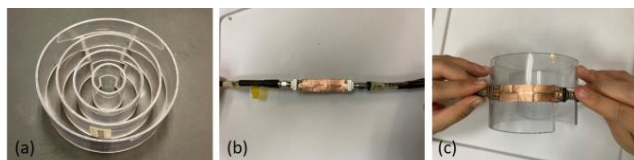


Figure 5. Experimental setup of the monotonic mandrel bending test: a) four sizes of polycarbonate cylindrical mandrels with outer radii of 4, 3, 2, and 1 in. that are used in the test; b) the flat configuration of microstrip line for VNA measurement; and c) the bending configuration of microstrip line for VNA measurement.

insertion loss change in the bending conditions. The insertion loss increases as the microstrip line samples experience the tensile strain at bending compared to the flat condition. As seen, the smaller the bending radius, the larger the strain, and the larger the increase in insertion loss. The 3-layer sample at the bending condition of bending radius of 1 in. (the smallest bending radius) has insertion loss ranging from 0.096 to 0.160 dB/mm for 20–40 GHz. For 6-layer sample at bending condition of bending radius of 1 in., the insertion loss is from 0.090 to 0.168 dB/mm. And for 9-layer sample at bending condition of bending radius of 1 in., the insertion loss is from 0.062 to 0.0143 dB/mm. At the smallest bending configuration, the 9-layer sample still shows the lowest loss, then the 6-layer sample, and then the 3-layer sample, as at the flat configuration. The increase in insertion loss due to bending are less than 0.037 dB/mm for 3-layer sample, 0.042 dB/mm for 6-layer sample, and 0.048 dB/mm for 9-layer sample. All the S_{21} measurements at bending taken in this set of bending tests are smaller than 0.2 dB/mm; therefore, all samples with three different metallization thickness can maintain good transmission at bending with bending radius greater than 1 in. In addition, all three flat measurements after bending tests almost overlap with the flat measurement taken before any bending. This indicates that there is very limited or negligible permanent damage in the ink structure due to the monotonic bending tests over these four different mandrels.

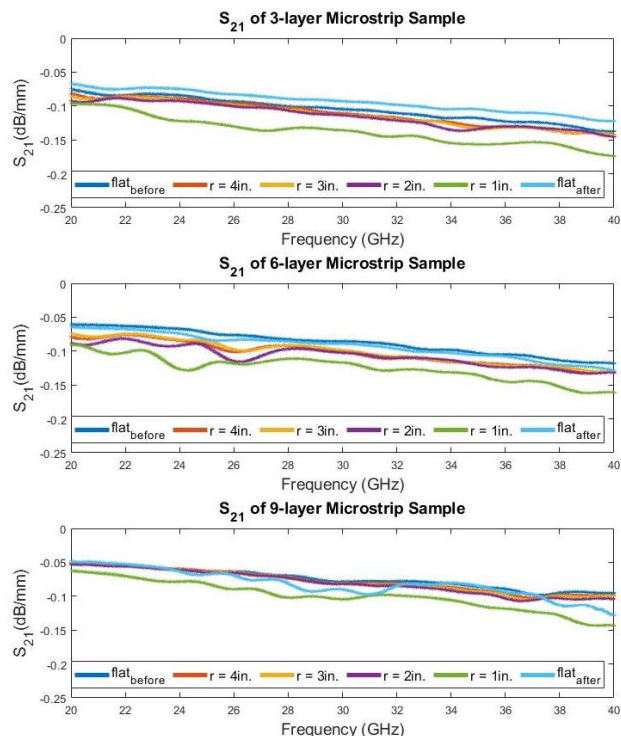


Figure 6. S_{21} measurement results of the monotonic mandrel bending test for one set of 3-layer, 6-layer and 9-layer sample.

B. Cyclic Mandrel Bending Test over Mandrel Size of radius of 1 in.

The reliability of the microstrip lines of different layer thickness is also studied using cyclic bending tests. An automated mandrel cyclic bending system is developed as seen in Fig. 7. The tested microstrip sample is clamped to the sample holder. The sample holder is attached to a rod-bearing system that would allow the sample holder to rotate freely, while the rod-bearing system is mounted on the rack-and-rail system that provides the sample holder with another degree of freedom in the longitudinal direction of the sample. Therefore, when the mandrel moves towards the sample from the original state in Fig. 7a to the bent state in Fig. 7b, the sample is fully conformed to the mandrel with minimum stretching. The size of the mandrel in this experiment is chosen to have radius of 1 in., since this is the smallest mandrel that used in the monotonic bending test and does not induce damage in the printed ink. Elastic cable is attached to the sample holder in horizontal direction to the end of the platform that would make sure the sample comes back to flat condition when the mandrel moves away from the sample to original state. The translational movement of the mandrel is controlled by the Arduino controller and realized by a motor-belt system attached to a sliding block on a rail. S_{21} measurement is taken while lying the sample flat on table before any bending test, and after tested number of cycles of cyclic bending.

Three sets of samples are used in the bending test, and each set includes a 3-layer, a 6-layer, and a 9-layer printed microstrip line sample. All nine samples are tested up to 10000 bending cycles. S_{21} is measured before any bending, after 1000, 5000, 7500, and 10000 cycles of bending. Fig. 8 presents the S_{21} measurement results for three different thicknesses of samples, and the results are the average values of the three sets. Fig. 8a plots the S_{21} measurements over the frequency range of 20-40 GHz after different numbers of bending cycles, while Fig. 8b plots the S_{21} at some key frequencies over the bending cycles.

It is seen that the insertion loss of the microstrip lines of all the samples increases, as the samples run through more bending cycles, and at all frequencies, the increased amount of insertion loss is similar. This change is expected, since greater numbers of bending cycles would induce fatigue

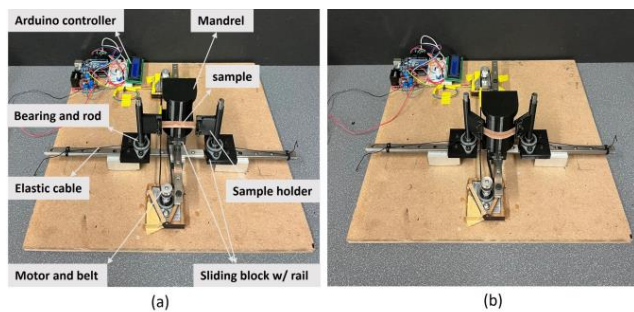


Figure 7. Experimental setup of the cyclic bending test: a) the sample is at the flat configuration; b) the sample is at the bending configuration.

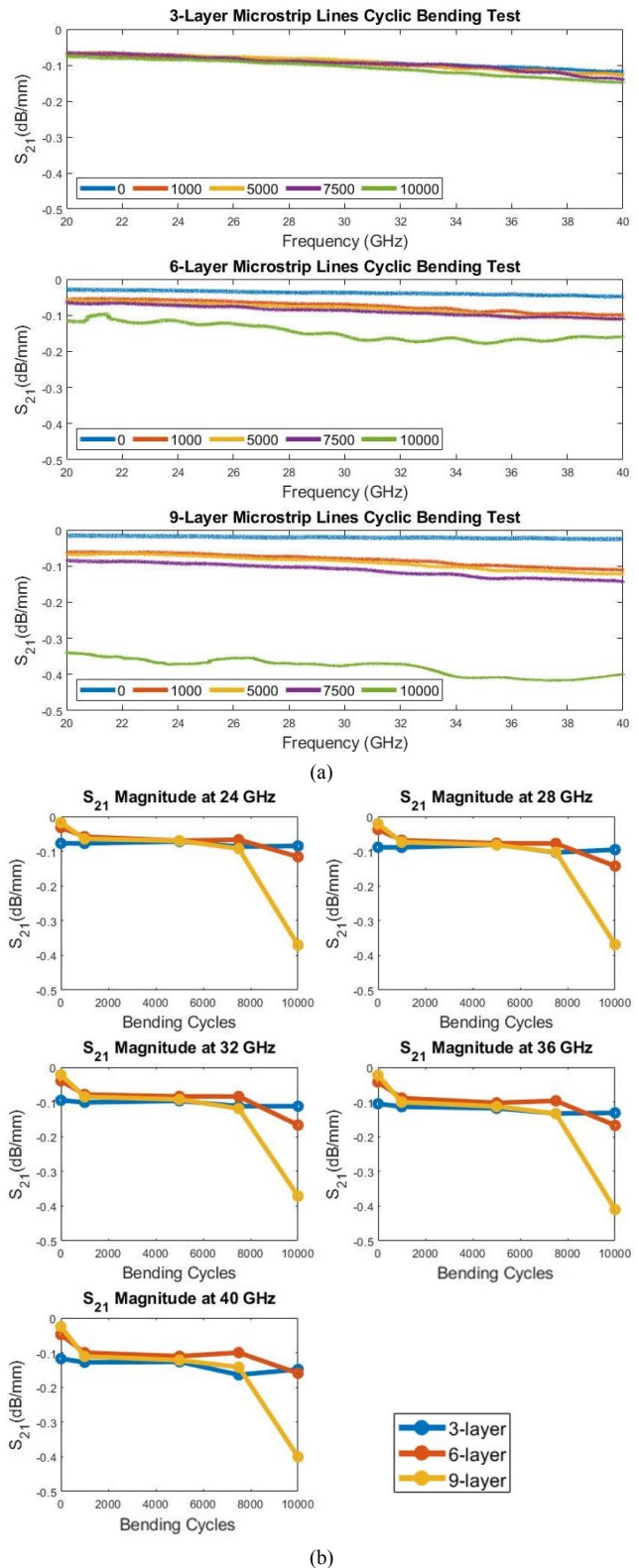


Figure 8. Average S_{21} measurement results of the cyclic mandrel bending test for three sets of 3-layer, 6-layer and 9-layer samples: a) insertion loss over 20-40 GHz, and b) insertion loss at key frequencies over bending cycles.

failures in printed ink structure. However, the amounts of change in insertion loss are different for different metallization thickness. For 3-layer microstrip line samples, insertion loss shows very limited change, which is less than 0.050 dB/mm up to 10000 bending cycles. But the insertion loss for both 6-layer samples and 9-layer samples significantly increases after 1000 cycles of bending, which is around 0.050 dB/mm and 0.080 dB/mm, respectively. In other words, before any bending, 9-layer samples have the least average insertion loss of 0.017–0.025 dB/mm for 20–40 GHz, 6-layer samples have about 0.020 dB/mm more loss, and 3-layer samples have additional 0.070 dB/mm more loss. After 1000 cycles of bending, 6-layer samples have the least insertion loss, while 9-layer samples become comparable to 3-layer samples. These relationships among three thicknesses of samples maintain up to bending cycles of 7500. When the bending test runs to 10000 cycles, the insertion loss of 6-layer samples increases to the level about 0.160 dB/mm, but 9-layer samples demonstrate around 0.400 dB/mm in loss, which is not considered as good transmission. In this case, 3-layer samples have the best electrical performance, followed by 6-layer samples, and then 9-layer samples. From this trend, it can be predicted that, 6-layer samples would fail after a few more thousands of bending cycles, while 3-layer samples would remain working for a longer time.

In summary, although 9-layer samples have the best electrical performance before any bending, they have the worst reliability as they feature very high loss after 10000 cycles of bending. For 3-layer samples, they have shown relatively stable S_{21} during bending cycles, but the conductivity is too low to provide good transmission and the insertion loss is mostly larger than 0.1 dB/mm especially at frequencies higher than 26 GHz. On the other hand, before

10000 bending cycles, 6-layer samples have been able to maintain an insertion loss smaller than 0.1 dB/mm for all frequency bands, therefore, they can be considered as the best option for inkjet printing silver traces, to achieve the balance between good electrical and mechanical reliability, for 5G and mm-wave flexible and wearable applications, using the fabrication process in this paper.

C. Scanning Electron Microscopy (SEM) Inspections

SEM images are taken before any bending, and after bending test at 1000 and 10000 cycles for one set of the microstrip samples that are run in the cyclic bending test. SEM images are taken at the same location on the samples to investigate the mechanical failure mechanism and process of printed microstrip line. The inspection results are presented in Fig. 9.

As indicated by the pre-bending SEM images that microstrip samples of different thicknesses have different printing quality to start with. The greater the number of layer, the more initial defects shown. This is because if the possibility of forming defects per printed area per layer is fixed, then printing more layers would result in higher chances to form local cracks. Also, since after each layer is printed, the printed structure is blown by the hot gun to limit ink spreading, greater number of printed layers means higher chance to form defects as the adhesion between layers is the weak point. Repeated use of hot guns after every layer can also be an issue, although such hot gun treatment is necessary to prevent ink spreading. After 1000 cycles of bending, it is seen that those pre-existing local defects start to grow perpendicular to the direction of bending for all three samples of different layer thickness. The crack growth in the 3-layer sample is less than 20 μm , and in the 6-layer sample, the crack growth is less than 50 μm . However, in the 9-layer

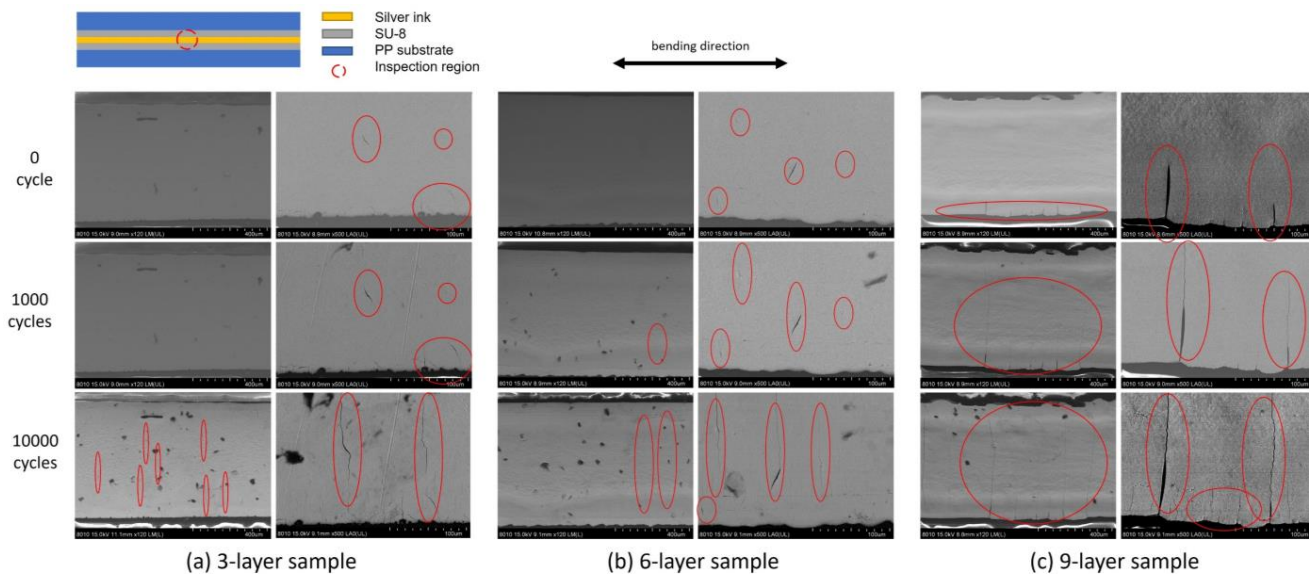


Figure 9. SEM images are taken before any bending, after 1000 cycles of bending, and after 10000 cycles of bending for: a) a 3-layer microstrip sample, b) a 6-layer microstrip sample, and c) a 9-layer microstrip sample.

sample, the crack growth is greater than 50 μm , and some of them is even longer than 400 μm . After 10000 cycles of bending, in the 3-layer microstrip sample, the cracks have grown to be around 1/3 of the microstrip line width (about 160 μm), and both cracks in the 6-layer sample and the 9-layer sample have grown into cross-sectional cracks, while the number of cracks is greater in the 9-layer sample than in the 6-layer sample. The observation found in SEM matches with the insertion loss measurements. The longer the crack growth after cyclic bending, the greater the insertion loss increase in the microstrip samples. When cross-sectional cracks are formed, there would be a significant increase in the insertion loss which would make the microstrip lines not transmitting.

D. Mechanical Finite-Element Analysis

The 3D FEA model is designed to mimic the mandrel bending test in ANSYS Workbench. Because of symmetry, a half-model is built as seen in Fig. 10 to save computational time. The model includes two major parts, the microstrip samples and the mandrel. The microstrip model is built based on the fabricated samples presented in Sec. II.B. The mandrel has a radius of 1 in. which is the mandrel size used in the cyclic bending test. The mechanical properties of materials for the simulation are shown in Table IV. For all materials, isotropic elastic material models are used in the simulations. The elastic modulus of silver ink and SU-8 is measured in-house using nanoindentation. The elastic modulus and Poisson's ratio of the PP are measured in-house by tensile testing. All other properties are obtained from literature. The mandrel is assumed to have a very high modulus to indicate its rigid nature in the simulation.

Fig. 10a shows the loading and constraint details of the mechanical simulation model. The four layers of the microstrip are modeled as one part. At the initial position, the left edge of the half-model, which is the center point of the whole substrate is simulated to be bonded to the mandrel as seen in Fig. 10a. To make sure that the sample could fully conform to the surface of the mandrel, a translational

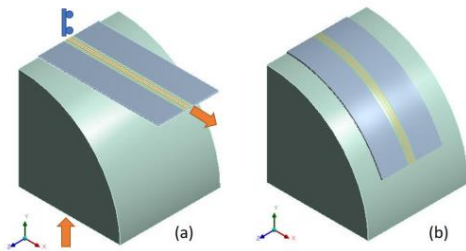


Figure 10. Half-model of mandrel bending mechanical simulation: a) initial position with loading and constraints condition, and b) final position.

TABLE IV. MATERIAL MECHANICAL PROPERTIES

Material	Young's Modulus (GPa)	Poisson's Ratio
Silver Ink	7.72 *	0.37 [27]
SU-8	2.65*	0.22 [28]
PP	0.23*	0.40 *
Copper	110.00 [29]	0.34 [30]

* measured in-house using nanoindentation for silver ink and SU-8, and tensile testing for PP.

displacement is applied to the mandrel with 0.2 mm per step through 15.8 mm when the entire sample is fully conformed to the mandrel as seen in Fig. 10b. Since this is a half-model, in the symmetrical plane, the motion is only allowed in the y-direction, while all other degrees of freedom are constrained. A small force of 0.5 N is applied to the end surface of the sample to keep the rest of the sample flat during bending procedure.

In the model, the mandrel is assumed as a rigid body in the simulation and is meshed with the 8-node SURF 154 elements of element size of 0.5 mm. The multi-layered microstrip is meshed with the 20-node SOLID 186 elements with element size of 0.1 mm. Through thickness, the silver ink layer has two elements, SU-8 layer two elements, PP layer four elements, and copper ground layer two elements.

Fig. 11 shows the first principal strain contours of the microstrip structure obtained from numerical simulation. The first principal strain contours are presented here to represent the bending strain, as their directions are along the bending direction. Although there is small variance in the geometry of thickness, overall width and base angle of the three microstrip samples, the strain contour shapes are similar as shown in Fig. 11. Major part of sample experiences constant strain as expected, since the mandrel has a constant radius of 1 in. Due to edge effect, and the fact that a small force is applied to the right end surfaces of the sample, there is some stress concentration occurs at the right end surfaces. Besides the rightmost portion of the samples, the maximum bending

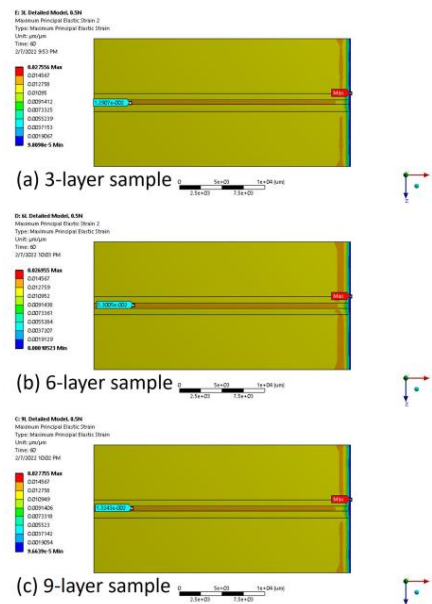


Figure 11. Mechanical simulation results of maximum principal strain distribution of microstrip line samples of a) 3 layers, b) 6 layers, and c) 9 layers of printed silver ink.

TABLE V. BENDING STRAIN VALUE IN SILVER INK LAYER

Sample	Hand-Calculation Value	Simulation Value
3-Layer	1.2212%	1.2907%
6-Layer	1.2344%	1.3005%
9-Layer	1.2551%	1.3245%

strain occurs at the silver ink structure which is the outmost layer, and the maximum values are different in different samples due to the thickness difference. The maximum bending strain in 3-layer sample is 1.2907%, in 6-layer sample is 1.3005%, and in 9-layer is 1.3245%. Bending strain at any location can be approximately computed by $\varepsilon = d/\rho$, where ε is the strain, d is the distance from the neutral axis of the multilayer structure and ρ is the bending radius at neutral axis. The difference in the maximum strain value in the silver ink layer between the numerical simulation and the bending strain calculation is 0.07% as shown in Table V.

Based on the above analysis, it can be concluded that in the bending experiments both monotonic and cyclic, the loading conditions to the 3-layer, 6-layer, and 9-layer samples are in the same level. Since the maximum strain values induced by bending over the mandrel with radius of 1 in. are fairly small in all three different thickness, no damage to the ink structures is expected, which matches with the observation in S_{21} measurements that the flat measurements of all three thickness before and after bending overlap with each other in the monotonic tests. In the fatigue cyclic testing, although the 3-layer, 6-layer, and 9-layer samples have similar global loading condition, the presence of small cracks would likely raise the local strain/stress value, and result in crack growth leading to both mechanical and electrical failure of the samples in shorter number of life cycles as seen in the cyclic bending test. As 9-layer samples have the worst printing quality to start with, they have the shortest life cycles.

IV. RAMP INTERCONNECT FABRICATION AND MEASUREMENTS

Traditional interconnects between chips and circuit board at mm-wave frequencies utilize ribbon or wire bonds. However, these methods introduce a long loop length, high parasitic inductance at higher frequencies and unintended radiation losses due to the high-arching bond wires [31]. Inkjet-printed interconnects feature a more rugged, planar, and conformal structure, which offers an improved RF performance even in challenging configurations. The ramp interconnects have been presented in previous work [10, 11], but in this paper, it is the first time that this structure has been implemented on a 3D printed flexible substrate and studied for its reliability.

The fabrication process and insertion loss of this ramp interconnect are first characterized using microstrip line structure. Two ramps are inkjet printed side by side with several SU-8 layers to bridge two transmission lines. A novel “staircase” method is used during the print so that 12 layers of square patterns with varying dimensions are printed layer by layer, as shown in Fig. 12a. This enables the height, length, and slope of the ramp to be adjustable based on different applications. The maximum height of the ramp for 12 layers of SU-8 is around 100 μm , which is the common thickness of dies at mm-wave frequencies. For each interconnect, a fine line that is 75 μm in width and 300 μm in length is inkjet

printed with silver ink onto the ramp. The measured S_{21} results are shown in Fig. 13a. Compared with the evaluation line without ramp interconnects, less than 0.5 dB degradation is added from each interconnect to the transmission line. Based on this result, an attenuator die (HMC651 from Analog Devices) is used to further test the functionality of this structure. The dimension of this die is shown in Fig. 12b, and the thickness is 100 μm . To fabricate the ramp interconnects to the die, first via holes are made with 200 μm drill on the substrate and conductive epoxy is used to fill the holes. Meanwhile, a small amount of epoxy is left on the surface of the substrate to attach the die. The end of the ramp is extended 30 μm to the edge of the die to help create a smooth transition for the interconnects. Then the interconnects are printed with silver ink in the form of 75 μm wide fine lines. Six layers of silver ink are printed in total to ensure good conductivity and reliable transition. Fig. 13b shows the S_{21} measurement results for inkjet printed ramp interconnects with the die. It can be seen that each ramp interconnect contributes less than 1.5 dB insertion loss to the attenuator die before 32 GHz. Further optimization is possible by tuning the dimension of the interconnects and the slope of the ramp.

Similar cyclic bending test is performed to evaluate the reliability of the ramp interconnect structure. To more accurately monitor the functionality change of the

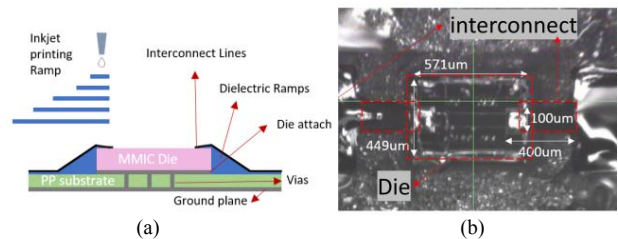


Figure 12. (a) 2D cross-section schematic of inkjet printed ramp interconnects for MMIC die on a 3D printed PP substrate; (b) top view of inkjet printed ramp interconnects with an attenuator die.

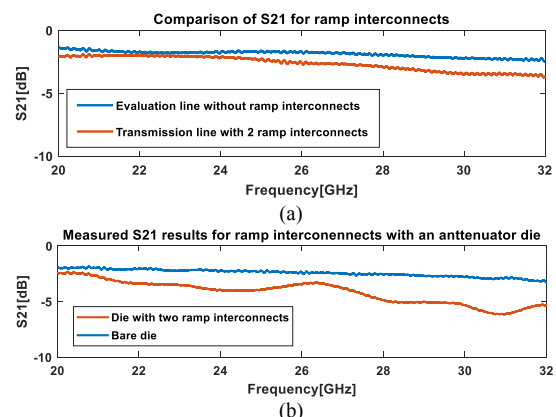


Figure 13. S_{21} measurement results for inkjet printed ramp interconnects with (a) evaluation lines and (b) an attenuator die.

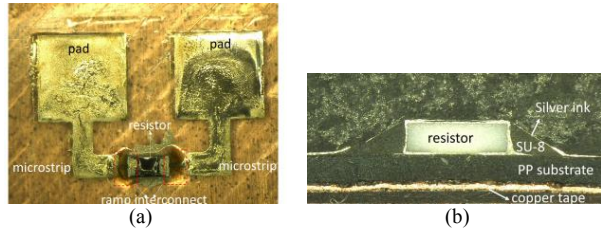


Figure 14. (a) Top view and (b) cross section of the tested structure of ramp interconnects built with a zero-ohm resistor.

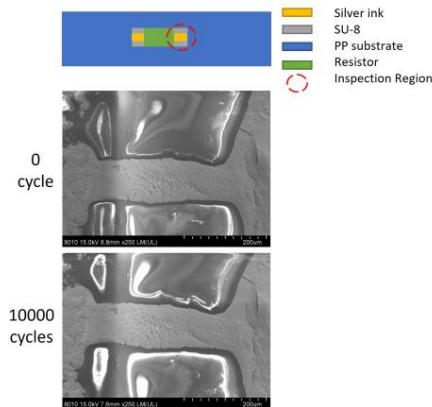


Figure 15. SEM images are taken before any bending, and after 10000 cycles of bending for the ramp interconnect.

interconnects, a zero-ohm resistor is used during the test as shown in Fig 14a and 14b. The zero-ohm resistor is 900 μm long, 450 μm wide, and 300 μm tall, and is placed in the center of the substrate. The resistor is also placed on a 60 mm long, and 15 mm wide PP substrate with copper tape as ground plane. The ramp interconnects are fabricated on both sides of the resistor and are connected to a short microstrip line of 1.5 mm long which is connected to a pad for resistance measurement. The bending test setup in Fig.7 is used for the bending reliability evaluation of the ramp interconnect with the mandrel of 1 in. radius. The resistance is measured at the two pads before any bending, and after 10000 cycles of bending. If the resistance largely increases or the circuit becomes open, the ramps may already break, and interconnects will no longer work. However, the resistance between the two pads remains the same at 3.5 Ω up to 10000 cycles of bending. In addition, the SEM images taken before any bending, and after 10000 cycles of bending indicate that there is no damage occurring at the interconnect during the bending as seen in Fig. 15.

V. CONCLUSION

This paper has demonstrated and tested the reliability of the inkjet printed microstrip lines of three different metallization thickness, and an inkjet printed 3D ramp interconnect on 3D printed PP substrate for 5G wearable applications. The microstrip lines are fabricated with 3 layers, 6 layers, and 9 layers of printed silver ink. All samples from the three thickness show good insertion loss value at flat condition, and thicker the silver ink structure smaller the

insertion loss. The maximum insertion loss over 20-40 GHz is 0.130 dB/mm for 3-layer samples, 0.101 dB/mm for 6-layer samples, and 0.080 dB/mm for 9-layer samples. One sample of each thickness is tested in the monotonic bending test over mandrels with radii of 4, 3, 2, and 1 in. As the mandrel size decreases, the strain induced on the silver ink structures increases, as well as the insertion loss of the microstrip lines of all thicknesses. At all bending conditions, the insertion loss of the microstrip lines is less than 0.170 dB/mm. Three samples of each thickness are tested in the cyclic bending test over the mandrel with radius of 1 in. up to 10000 cycles. 9-layer samples can maintain good transmission properties up to 7500 cycles, while 3-layer and 6-layer samples can survive up to 10000 cycles. The increase in insertion loss is found to be the largest in 9-layer samples, and smallest in 3-layer samples. Initial defects from fabrication are found in the ink from SEM images, as 3-layer has the least and 9-layers the most. SEM images are also taken after 1000 and 10000 cycles of bending, which show cracks growing from the pre-existing defects. Longer cracks and more cracks, lead to greater increase of insertion loss of the microstrip lines. Mechanical FEA simulation indicates that the loading conditions of all three thicknesses are among the same level of 1.3% bending strain. Therefore, initial printing quality plays the most important role in controlling the fatigue reliability of the printed microstrip lines. The optimal metallization thickness for inkjet printed electronics on 3D printed PP substrate based on current fabrication process is 6 layers of silver ink, which can balance the electrical performance and mechanical reliability for 5G and mm-wave flexible and wearable applications. Ramp interconnects are designed and fabricated with transmission lines and an attenuator die onto PP substrate. SU-8 is inkjet printed layer by layer to create ramps with smooth transition to overcome the height difference between the die/resistor and substrate, so that the interconnects can be inkjet printed with silver ink to connect the die/resistor to transmission lines on the substrate. Preliminary bending test result indicates the ramp interconnect structure has good reliability at the bending radius of 1 in. The tested structure has no change in physical structure or functionality up to 10000 cycles of bending.

The life cycles of 3-layer and 6-layer microstrip samples will be further studied in cyclic bending test. This work has quantified the insertion loss of the interconnects, and in the future, the resistance/resistivity change of the printed ink structure and other RF parameters will be quantified. Further reliability evaluations will be also performed on ramp interconnects with smaller bending radii.

ACKNOWLEDGMENT

This material is based on research sponsored by Army Research Laboratory under agreement number W911NF-19-2-0345. The U.S. Government is authorized to reproduce and distribute reprints for Government purposes notwithstanding any copyright notation thereon. The views and conclusions contained herein are those of the authors and should not be

interpreted as necessarily representing the official policies or endorsements, either expressed or implied, of Army Research Laboratory (ARL) or the U.S. Government.

REFERENCES

- [1] J. G. Andrews et al., "What Will 5G Be?," in *IEEE Journal on Selected Areas in Communications*, vol. 32, no. 6, pp. 1065-1082, June 2014, doi: 10.1109/JSAC.2014.2328098.
- [2] Niu, Y., Li, Y., Jin, D. et al. A survey of millimeter wave communications (mmWave) for 5G: opportunities and challenges. *Wireless Netw* 21, 2657–2676 (2015). <https://doi.org/10.1007/s11276-015-0942-z>
- [3] I. Ndiip and K. Lang, "Roles and Requirements of Electronic Packaging in 5G," *2018 7th Electronic System-Integration Technology Conference (ESTC)*, 2018, pp. 1-5, doi: 10.1109/ESTC.2018.8546469.
- [4] N. F. M. Aun, P. J. Soh, A. A. Al-Hadi, M. F. Jamlos, G. A. E. Vandenbosch and D. Schreurs, "Revolutionizing Wearables for 5G: 5G Technologies: Recent Developments and Future Perspectives for Wearable Devices and Antennas," in *IEEE Microwave Magazine*, vol. 18, no. 3, pp. 108-124, May 2017, doi: 10.1109/MMM.2017.2664019.
- [5] R. R. Tummala, "Moore's law meets its match (system-on-package)," in *IEEE Spectrum*, vol. 43, no. 6, pp. 44-49, June 2006, doi: 10.1109/MSPEC.2006.1638044.
- [6] Yin, Z., Huang, Y., Bu, N. et al. Inkjet printing for flexible electronics: Materials, processes and equipments. *Chin. Sci. Bull.* 55, 3383–3407 (2010). <https://doi.org/10.1007/s11434-010-3251-y>
- [7] N. Shahrubudin, T. C. Lee, and R. Ramlan, "An overview on 3D printing technology: Technological, materials, and applications," *Procedia Manufacturing*, vol. 35, pp. 1286–1296, 2019.
- [8] S. H. Ko, H. Pan, C. P. Grigoropoulos, C. K. Luscombe, J. M. Fréchet, and D. Poulidakos, "All-inkjet-printed flexible electronics fabrication on a polymer substrate by low-temperature high-resolution selective laser sintering of metal nanoparticles," *Nanotechnology*, vol. 18, no. 34, p. 345202, 2007.
- [9] A. O. Watanabe, M. Ali, S. Y. Sayeed, R. R. Tummala, and M. R. Pulugurtha, "A review of 5G front-end systems package integration," *IEEE Transactions on Components, Packaging and Manufacturing Technology*, vol. 11, no. 1, pp. 118–133, 2021.
- [10] X. He, B. K. Tehrani, R. Bahr, W. Su and M. M. Tentzeris, "Additively Manufactured mm-Wave Multichip Modules With Fully Printed "Smart" Encapsulation Structures," in *IEEE Transactions on Microwave Theory and Techniques*, vol. 68, no.7, pp. 2716-2724, July 2020, doi: 10.1109/TMTT.2019.2956934.
- [11] Tehrani, B., R. Bahr and M. Tentzeris. "Inkjet and 3D Printing Technology for Fundamental Millimeter-Wave Wireless Packaging." *Journal of microelectronics and electronic packaging 2017 (2017)*: 000252-000257.
- [12] J. H. Chow, S. K. Sitaraman, C. May and J. May, "Study of Wearables with Embedded Electronics Through Experiments and Simulations," *2018 IEEE 68th Electronic Components and Technology Conference (ECTC)*, 2018, pp. 814-821, doi: 10.1109/ECTC.2018.00126.
- [13] J. H. Chow, J. Meth and S. K. Sitaraman, "Twist Testing for Flexible Electronics," *2019 IEEE 69th Electronic Components and Technology Conference (ECTC)*, 2019, pp. 785-791, doi: 10.1109/ECTC.2019.00124.
- [14] R. Chen, J. H. Chow, Y. Zhou, J. S. Meth and S. K. Sitaraman, "Cyclic Bending Effects on Resistance of Screen-Printed Silver Conductors," in *IEEE Transactions on Components, Packaging and Manufacturing Technology*, vol. 11, no. 11, pp. 1877-1888, Nov. 2021, doi: 10.1109/TCPMT.2021.3108491.
- [15] Y. Zhou, S. Sivapurapu, M. Swaminathan and S. K. Sitaraman, "Mechanical and High-Frequency Electrical Study of Printed, Flexible Antenna Under Deformation," in *IEEE Transactions on Components, Packaging and Manufacturing Technology*, vol. 10, no. 7, pp. 1088-1100, July 2020, doi: 10.1109/TCPMT.2020.2995532.
- [16] I. A. Bower, C. L. Taylor, and S. K. Sitaraman, "Study of inkjet-printed serpentine structure on flexible substrates deformed over sculptured surfaces," *Flexible and Printed Electronics*, vol. 5, no. 1, p. 015010, 2020.
- [17] B. Stewart and S. Sitaraman, "Biaxial inflation stretch test for printed flexible electronics," *Advanced Engineering Materials Advanced Engineering Materials*, 2021.
- [18] R. Chen, J. H. Chow, Y. Zhou, J. S. Meth and S. K. Sitaraman, "Cyclic Bending Effects on Resistance of Screen-Printed Silver Conductors," in *IEEE Transactions on Components, Packaging and Manufacturing Technology*, vol. 11, no. 11, pp. 1877-1888, Nov. 2021, doi: 10.1109/TCPMT.2021.3108491.
- [19] R. Chen, J. H. Chow, C. Taylor, J. Meth and S. K. Sitaraman, "Mechanical and Electrical Behavior of Printed Silver Conductor in Adaptive Curvature Flexure Test," in *IEEE Transactions on Components, Packaging and Manufacturing Technology*, vol. 10, no. 5, pp. 806-816, May 2020, doi: 10.1109/TCPMT.2020.2985649.
- [20] R. Chen, J. Chow, C. Taylor, J. Meth and S. Sitaraman, "Adaptive Curvature Flexure Test to Assess Flexible Electronic Systems," *2018 IEEE 68th Electronic Components and Technology Conference (ECTC)*, 2018, pp. 236-242, doi: 10.1109/ECTC.2018.00044.
- [21] S. Sivapurapu et al., "Multi-Physics Modeling and Characterization of Components on Flexible Substrates," in *IEEE Transactions on Components, Packaging and Manufacturing Technology*, vol. 9, no. 9, pp. 1730-1740, Sept. 2019, doi: 10.1109/TCPMT.2019.2931452.
- [22] Y. Zhou et al., "Study of Electrical and Mechanical Characteristics of Inkjet-Printed Patch Antenna Under Uniaxial and Biaxial Bending," *2019 IEEE 69th Electronic Components and Technology Conference (ECTC)*, 2019, pp. 1939-1945, doi: 10.1109/ECTC.2019.00298.
- [23] S. Sivapurapu et al., "Multi-physics Modeling Characterization of Aerosol Jet Printed Transmission Lines," *2018 IEEE MTT-S International Conference on Numerical Electromagnetic and Multiphysics Modeling and Optimization (NEMO)*, 2018, pp. 1-4, doi: 10.1109/NEMO.2018.8503509.
- [24] N. Aslani Amoli et al., "Screen-Printed Flexible Coplanar Waveguide Transmission Lines: Multi-physics Modeling and Measurement," *2019 IEEE 69th Electronic Components and Technology Conference (ECTC)*, 2019, pp. 249-257, doi: 10.1109/ECTC.2019.00044.
- [25] S. Sivapurapu et al., "Flexible and Ultra-Thin Glass Substrates for RF Applications," *2021 IEEE 71st Electronic Components and Technology Conference (ECTC)*, 2021, pp. 1638-1644, doi: 10.1109/ECTC32696.2021.00260.
- [26] "Understanding VNA Calibration", 2012. [Online]. Available: http://anlage.umd.edu/Anritsu_understanding-vna-calibration.pdf [Accessed 18 Jan. 2019].
- [27] E. Lam, "Fabrication and Material Characterization of Silver Cantilevers via Direct Surface Micromachining", Undergraduate, Massachusetts Institute of Technology, 2005.
- [28] Stephan Keller et, "Processing of thin SU-8 films", al 2008 J. Micromech. Microeng. 18 125020
- [29] D. Yu and F. Spaepen, "The yield strength of thin copper films on Kapton", *Journal of Applied Physics*, vol. 95, no. 6, pp. 2991-2997, 2004.
- [30] J. Zhu, J. Feng and Z. Guo, "Mechanical properties of commercial copper current-collector foils", *RSC Adv.*, vol. 4, no. 101, pp. 57671-57678, 2014
- [31] T. Krems, W. Haydl, H. Massler, and J. Rudiger, "Millimeter-wave performance of chip interconnections using wire bonding and flip chip," in *IEEE MTT-S Int. Microw. Symp. Dig.*, vol. 1, Jun. 1996, pp. 247–250